Photosensor test station for the Mu2e electromagnetic calorimeter

G. PEZZULLO on behalf of the MU2E CALORIMETER group

INFN, Sezione di Pisa and Università di Pisa - Pisa, Italy

Summary. — The Mu2e experiment searches for coherent, neutrinoless conversion of muons into electrons in the field of a nucleus. The Mu2e measurement will have a sensitivity of fews parts in 10^{-17}, with an improvement of a factor of 10^3–10^4 with respect to the existing limits. The Mu2e apparatus takes advantage of the high intensity muon beam which hits muon stopping targets, and uses a detector composed of a low-mass straw tubes tracker and an electromagnetic calorimeter. The calorimeter is made of 1860 hexagonal crystals read out by two large area photosensors, for a total of 3720 channels. Two options of photosensors are currently under study: large-area Avalanche Photo Diodes (APDs) and Silicon Photo Multipliers (SiPMs). A photosensor test station has been developed in Pisa, in collaboration with the LNF Mu2e group, in order to validate the photosensors performance. In particular the following characteristics are carefully studied: gain *vs.* bias voltage, gain *vs.* temperature, gain *vs.* light source position and dark current characterization.

PACS `29.40-Vj` – Calorimeters.
PACS `29.90.+r` – Other topics in elementary-particle and nuclear physics
　　　　　　　　experimental methods and instrumentation.

1. – Mu2e physics

Several experiments of the last decades proved that lepton-flavor-violation (LFV) for neutral leptons (neutrinos) is a fact. This implies that also charged LFV (cLFV) is possible, but with a rate not yet reached by the current experimental sensitivity. An observation of a cLFV signal would be an unambiguous evidence of new physics. A method to search for cLFV exploits muons; so far two processes involving muons have been studied: $\mu \to e\gamma$ and $\mu N \to eN$. The current upper limits for these two processes are: $BR(\mu \to e\gamma) < 5.7 \times 10^{-13}$ [1] and $R_{\mu e}$(Au targets) $< 7 \times 10^{-13}$ [2]. Compared to $\mu \to e\gamma$, the rate of $\mu N \to eN$ is scaled by a factor of $\sim \alpha Z^2$, as the photon becomes virtual and couples with the nucleus. Due to the interaction with the nucleus, additional new physics processes can contribute to $\mu N \to eN$ compared to $\mu \to e\gamma$, the ones with a contact term or a four-fermion interaction, such as compositeness or lepto-quarks [3]. The search for muon conversion has a clear signature to look for. Indeed in the muon
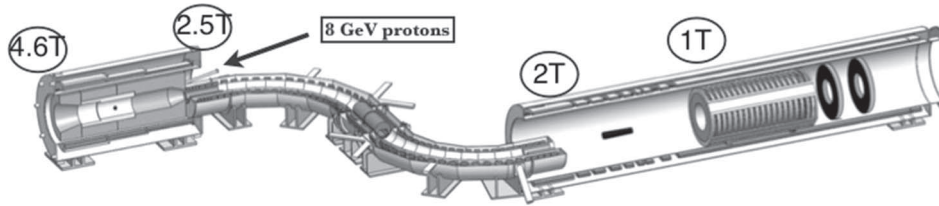
Fig. 1. – Mu2e experimental layout. The Cosmic ray veto is not shown.

conversion process the initial state is a muonic atom that makes a transition to a 2-body state consisting of a mono-energetic electron recoiling to the atomic nucleus, with no neutrinos in the final state and no nucleus breakup. The nucleus is not observed while the conversion electron (CE) has an energy of the muon rest mass minus small corrections for the recoil and the binding energy of the muon.

2. – The Mu2e apparatus

The Mu2e experiment [4] is composed by three main superconducting magnet systems (see fig. 1). The first is the production solenoid (PS) where an intense 8 GeV proton beam (pulsed with a period of ~ 1800 ns) strikes a tungsten target producing mostly π's. A graded magnetic field (from 2.5 to 4.6 T) then collects most of the produced charged particles and moves them through the second magnet, the transport solenoid (TS). The TS is dedicated to move and select only negative low-momentum muons through the last solenoid, the detector solenoid (DS). Such a selection is done by means of a system of collimators at the sides and in the middle of the TS. The S shape of the transport solenoid allows also to avoid that all neutral particles generated in the PS reach the DS. The DS is the solenoid where the muon beam arrives, stops on the target and the reaction products are analized by the detectors. In order to do that, it houses the muon stopping targets (Al) and the detection system devoted to identify and analyze the conversion electrons (CE). The Al targets reside in a graded field region that varies from 2 to a 1 T, so that electrons emitted upstream are reflected downstream through the detectors region. Downstream the targets a proton absorber, made of high density polyethylene is located to reduce the proton flux (produced in nuclear reactions) to the tracker. The tracking system consists of 20 straw tubes stations designed for maximizing the acceptance and the precise reconstruction of the CE. This is the main detector of the experiment and it is expected to get a resolution of ~ 120 keV/c for 100 MeV/c momentum. The second detector adopted is a crystal electromagnetic calorimeter (EMC) that will be described in details in the next section. A Cosmic Ray Veto (CRV) system surrounds the DS on three sides (the ground is not covered) and extends up to the midpoint of the TS; it consists of four layers of extruded scintillator bars with embedded wavelength shifting fibers read out with Silicon photomultipliers (SiPMs). The Veto signal corresponds to coincident hits in three out of four layers. It is designed to reduce the number of expected cosmic induced background events to 0.05 events during the entire running period (three years). In the region of the muon stopping target the CRV is expected to be 99.99% efficient. Neutron shields, made of concrete blocks, are also present between the DS and the CRV to reduce the neutron flux (coming from the muon stopping targets) which otherwise can compromise the efficiency and functionality of the CRV.

TABLE I. – *Calorimeter configurations studied for optimizing the geometry.*

Crystal apothem [cm]	Disk radii [cm]	# crystal	Crystal volume [cm^3]	Efficiency [%]
1.55	35.91/64.3	996	168.8×10^3	90.5 ± 0.6
1.55	35.91/67.23	1110	193.9×10^3	90.4 ± 0.6
1.6	34.01/66.35	1044	194.4×10^3	92.2 ± 0.6
1.6	37.1/66.35	966	179.8×10^3	90.2 ± 0.6
1.65	35.1/66.0	930	184.1×10^3	92.2 ± 0.6
1.7	36.12/64.73	798	167.7×10^3	90.4 ± 0.6

3. – The Mu2e calorimeter

3.1. *Calorimeter requirements*. – The Mu2e calorimeter should confirm that the candidates reconstructed by the extremely precise tracker system are indeed conversion electrons while performing a powerful mu/e particle identification. Moreover, it should provide a high-level trigger for the experiment, independently of the tracker system, to bring the rate on disk to $\sim$ few kHz. The calorimeter should also be able to keep functionality in an environment where the background delivers a dose of ~ 12 krad/year in the hottest area and to work in the presence of 1 T axial magnetic field. The calorimeter will also help on selecting correct hits in the tracker. All these requirements translate into the following parameters to be satisfied by the Mu2e calorimeter:

  – provide a large acceptance for electron and positron tracks,

  – determine the energy with a resolution better than 5% at 100 MeV,

  – reconstruct the time with a resolution ≤ 0.5 ns,

  – reconstruct the impact position with a resolution better than ~ 1 cm.

The calorimeter should survive in the Mu2e environment where a radiation dose of 100 Gy/year/crystal is expected in the hottest areas. Moreover, the calorimeter is embedded in the DS where a 1 T magnetic axial field exists.

3.2. *Calorimeter design*. – The calorimeter design consists of two disks whose dimension have been optimized by simulating signal electron events with the official Mu2e framwork [5]. Simulation results (see table I) shows that the calorimeter acceptance gets its maximum with an inner (outer) radius of 35.1 (66) cm.

Figure 2 shows that the optimum disks separation is 75 cm, which is $\sim \frac{1}{2}$ wavelength of the signal electron helix.

Each disk is composed by ~ 930 BaF$_2$ hexagonal crystals, see fig. 3, with a length of 20 cm and a distance among flats of 1.65 cm. The readout system is constitued by two large area APDs, in order to grant a better light yield while providing redundancy of the readout system.
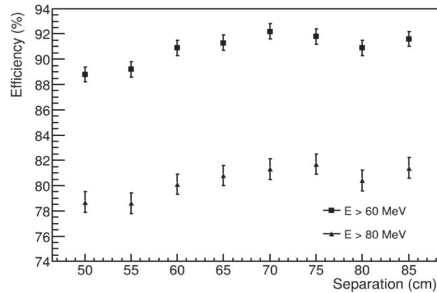
Fig. 2. – Calorimeter acceptance *vs.* the disk separation.
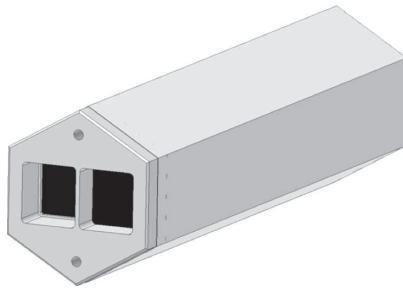
Fig. 3. – Crystal shape with APDs boxes colored in black.

3˙3. *Crystal choice*. – In the Conceptual Design Report [4] the calorimeter baseline choice was based on LYSO crystals. Since then, estensive R&D program has been carried out on this option and test beams [6] and electronic design were tuned accordingly. However, during the last year, and despite an active R&D program at Caltech, in cooperation with SICCAS and SIPAT, aiming to reduce the commercial price of LYSO crystals, the large increase in Lu_2O_3 salt price over the past two years has made the cost of a LYSO calorimeter unaffordable.

BaF_2 as been selected as baseline because it presents several advantages:

– it has a small decay time of the fast component,

– it is not hygroscopic,

– It is rad hard.

However BaF_2 presents also some drawbacks and difficulties. In particular, the fast component is emitted in the deep UV region at 220 nm (see fig. 4) and, moreover, there is a large component (peaked at 300 nm) that has a long decay time of 650 ns. Name of the game for this crystal is to find an adequate photosensor.

3˙4. *Photosensor choice*. – There are not existing photosensor candidates for BaF_2 readout that could have a high quantum efficiency at 220 nm while working in the presence of 1 T magnetic field. Photomultipliers are excluded. Channel plate PMTs are at present far too expensive, although spinoffs from the LAPPD project are still being pursued. Our main thrust, however, is to use solidi state photosensors, either APDs, SiPMs or MPPCs, with extended UV response. APDs and MPPCs from Hamamatsu and RMD
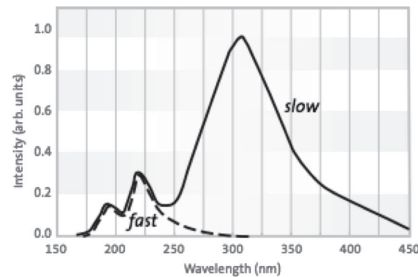
Fig. 4. – BaF$_2$ emission spectrum.
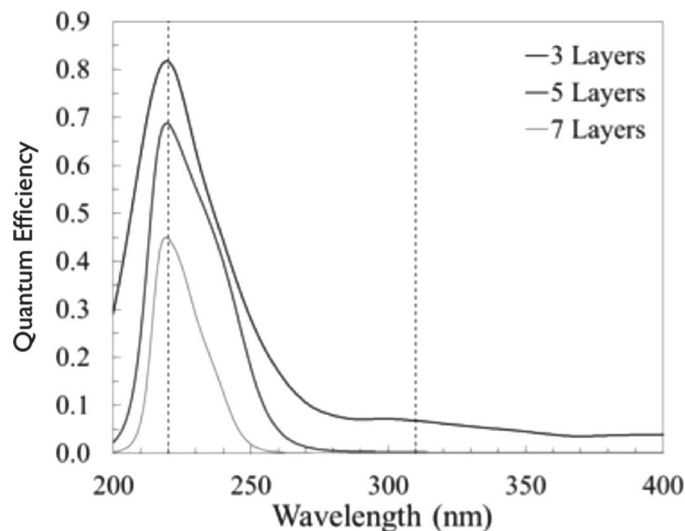
Fig. 5. – QE *vs.* wavelength of 3 different samples of APDs with different number of atomic layer deposition. The lighter-grey line represents the selected APD.

made without the normal protective epoxy coating, and therefore somewhat fragile, can have quantum efficiencies in the 200 nm region of $\sim 17\%$, but do not discriminate between the 220 nm fast component and 300 nm slow component of BaF$_2$. The presence of the slow component limits the rate capability of the calorimeter, and can therefore be an issue in high-background conditions. We are pursuing an experimental R&D approach to both improving the photosensor quantum efficiency and the slow component discrimination. A Caltech/JPL/RMD consortium has been formed to develop a modified RMD large-area APD into a delta-doped superlattice APD. This device will also incorporate an atomic layer deposition antireflection filter that will provide 60% quantum efficiency at 220 nm and $\sim 0.1\%$ efficiency at 300 nm, thereby enabling us to not only have a larger number of photoelectrons/MeV ($\times 3$), but also to take full advantage of the fast decay time component of BaF$_2$. The greatly reduced undepleted region of this device will also result in substantially improved rise time of the device.

Conventional RMD APDs will be thinned to remove the surface and undepleted region before the avalanche layer, and the superlattice structure and optimized antireflection coating will then be deposited at the JPL Microdevices Lab. Figure 5 shows the
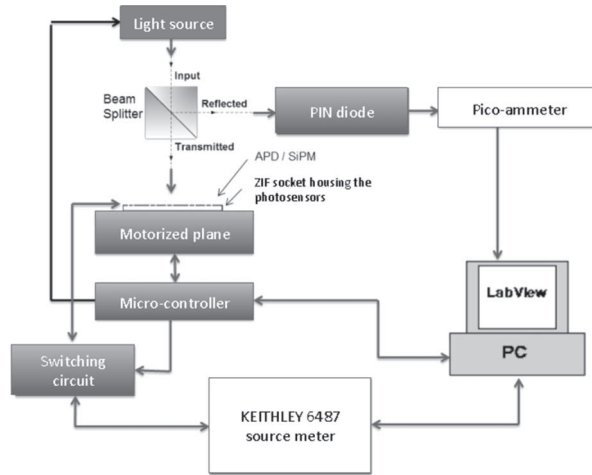
Fig. 6. – Scheme of the test station.

calculated QE response of the resulting APD as a function of wavelength. For a five-layer AR coating, the QE at the fast component of BaF2 is nearly 70%, and the extinction at the slow component wavelength is nearly complete.

4. – The photosensor test station

The Mu2e calorimeter is equipped by 3840 photosensors, so an automated test station is necessary for testing all of them by groups. The photosensor choice affects only two parts of the station design: the light source of the optical system and the bias voltage needed by the photosensors. In fact RMD-APDs need $\sim 1000\,\text{V}$ and UV laser, instead SiPMs need low voltages ($\sim 40\,\text{V}$) and pulsed LED light sources. For each photosensor both functionality and gain must be tested. The station operates the following measures:

  – gain (G) as a function of both bias voltage and temperature,

  – quantum efficiency *vs.* the wavelength of the incident light,

  – excess noise factor (F) *vs.* the gain.

The presented test station is composed by the following elements: a light source, one PCB housing a matrix of photosensors to be tested, a motorized plane, a micro-controller, one source meter Keithley 6487, one calibrated PIN diode. Figure 6 shows a sketch of the project.

The zero insertion force (ZIF) socket housing the photosensor is supported by the motorized plane, which allows to move the socket itself by steps with a precision better than fraction of mm behind the light source used to stimulate the photosensors. Plane movements are controlled by a system of two stepper motors and two absolute encoders. Two couples of limit-switches, one for each direction, are also used for limiting the movements of the plane.

The optical system is constituted by a light source, a beam splitter and a PIN diode. The light source depends on which photosensor one needs to test; for RMD-APDs a
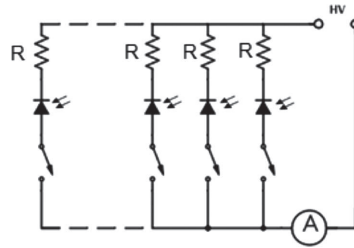
Fig. 7. – Simplified scheme of the switch circuit.

deuterium lamp can be used for reaching the deep-UV region where the photosensor needs to be tested. It must be equipped with optical filters for selecting the wavelength where one wants to test the APD. Instead for SiPM the solution is represented by a standard RGB "red-green-blue" diode, driven via "pulse width modulation" (PWM). The PIN diode selected for the station is the PDA25K-EC [7], which has a wide response in the range [160, 500] nm and is also already amplified. The PIN diode is necessary during the operation test for monitoring the light source intensity.

The Keithley 6487 is a source meter which supplies the bias voltage for the photosensor under test and also measures the current which exits from the device itself. Figure 7 shows the scheme of the switching circuit which allows to select the device to test.

The fotosensor gain depends strongly by the temperature, so the test station needs both to operate in a climatic station and to be equipped with temperature sensors for the ring control. Moreover the station must be entirely covered, to avoid light contamination which could lead on a fake response of the photosensors.

The test station will be controlled by a LABVIEW software. A micro-controller is necessary for driving the motorized plane movements, the light source and the switching circuit. The PIC24FJ12GA010 represents a good candidate, which satisfies all the requirements. Figure 8 shows the mechanical part of the station, which has been re-used from a old station assembled at the INFN of Pisa in 1999 for testing the modules of the Si detector of the CDF experiment at Fermilab [8]

It is constituted by

  – two stepper motors PH299-E4.0 B,

  – two absolute encoders ELCIS LA390- G4096-5-CM5-R,

  – two limit switch for each direction HONEYWELL S&C BZ series.

A commercial driver G203V [9] has also been adopted for controlling the stepper motors via the micro-controller.

In the next two sections there follow the description of the encoder board interface developed for reading the encoders and then the description of the firmware used for driving the motorized plane.

4˙1. *Encoder board interface*. – The PIC24FJ128GA010 (PIC-master) does not have all the pins supporting 5V, which is needed for reading the output signal of the encoders. So a simple board has been developed as an external interface between the PIC-master and the two encoders. The designed board uses a serial protocol to transfer the data to the PIC-master. The two encoders used in the station are quite old and they use a
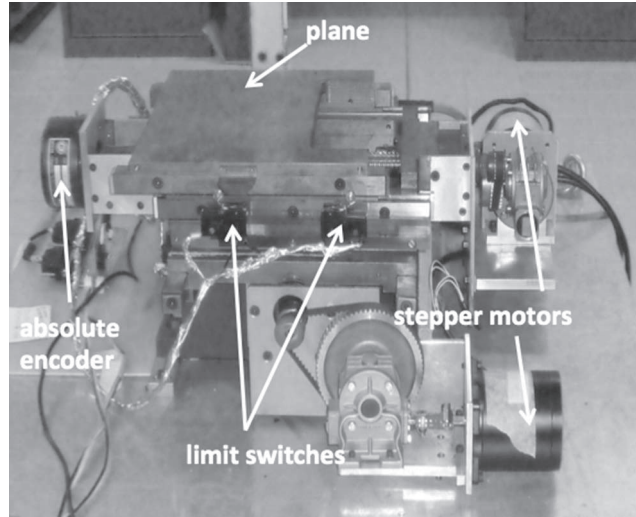
Fig. 8. – Mechanical structure of the motorized plane.
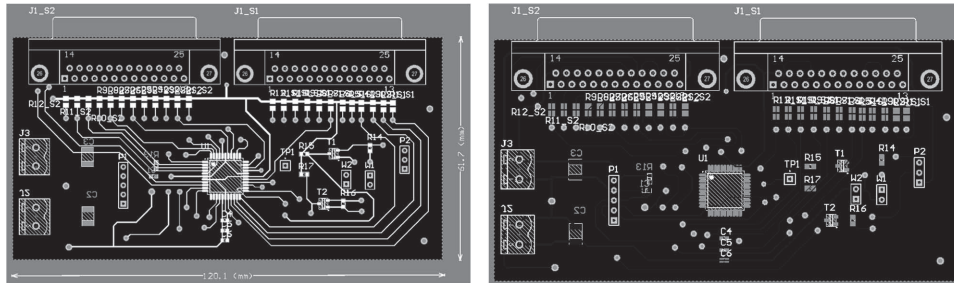
Fig. 9. – Top (left) and bottom (right) views of the PCB layout.

parallel output at 12 but, composed by transistor NPN open collector with a bias voltage at 5V. That implies that each output needs a pull-up resistor for each pin. The function of this board is to read the 24 bit at 5V from the encoders and transfer the data to the PIC-master via serial port. The dsPIC30F4013 [10] (PIC-slave) has been selected for operating these functions because it presents several advantages: it operates at 5V, it is very similar to the PIC-master, but with less resources.

Figure 9 shows the top and bottom views of the board layout. The connector P1 is used for programming the PIC-slave, instead J2 and J3 connectors are used for the bias voltages at 3.3 V for the pull-up of the Bus I^2C and 5V for the PIC-slave itself. The way this board operates is very simple: essentially it stays in pending mode until an instruction is transferred by the PIC-master, then it transmits the encoders information. The PIC-master can drive only two functions:

  – *initialize the encoders*: return the initial positions of the encoders,

  – *read the encoders*: read the position of the two encoders.

By these two functions the PIC-master is able to calculate the movements of the plane on each direction.

Fig. 10. – Comparator mounted on one of the two side of the motorized plane.

4˙2. *Motorized plane firmware*. – The photosensors active area is of about $100\,\mathrm{mm}^2$, so for testing their homogeneity in the response the light source must be fired in several positions of the photosensor. So a precision of about $0.5\,\mathrm{mm}$ on the movements on each axis of the motorized plane is needed for the correct characterization. Naively the presented apparatus is supposed to satisfy this requirement, in fact the encoders used have 12 bit precision and $5\,\mathrm{mm}$ step, so their expected resolution is of about $5000/4096\,\mu\mathrm{m} \sim 1.2\,\mu\mathrm{m}$. Obviously the final resolution will be slightly worst, because experimental effects must be taken into account.

The explorer 16 Development Board [11], which mounts the PIC24FJ128GA010, has been used to develop and test the firmware. As described in the previous sections, the motorized plane movements is controlled by two stepper motors, driven by the PIC-master via two G203V drivers. The PIC-master takes advantage of 5 modules PWM for controlling the drivers. A sequence of pulses generated by the PIC-master can control both number of steps and velocity just by a correct setting of both frequency and duty cycle of pulses.

First of all the transmission rate of the stepper motors has been measured in order to calibrate properly the pulses used for moving them. Then the firmware has been developed dividing it into two main functions:

1. *init_motor*: initialize the system and moves the plane at the origin position,

2. *got_to(x, y)*: moves the plane in the position $(x,\ y)$ passed as argument of the function itself.

After these two functions have been written, a protocol for the serial communication between the PC and the board Explorer 16 has been developed, such to have the possibility of driving the system via PC. That was possible thanks to a Universal Asynchronous Receiver Transmitter already present on the PIC-master and a RS232 cable used for linking the PC with the board Explorer 16.

The final test of the firmware has been performed using two comparators, as shown in fig. 10, for measuring movements less than 1 cm, and a bore for measuring movements up to 18 cm. Both series of measurements proved that the movement precision is better than $\sim 40\,\mu$m, which largely satisfies the requirement of the project.

5. – Conclusions

This test station represents an important step for the building of the Mu2e calorimeter, because it guarantees the correct functionality of the photosensor that will be mounted. In this paper the controller and the structure of the mechanical part have been presented.

All the electronics which concern the micro-controller used for the motorized plane have been developed, thanks to the board Explorer 16 and a custom board for communicating with the two encoders.

The functionality and the performance of the firmware satisfy the requirement set by the project. Tests demonstrated that a precision better than $\sim 40\,\mu$m can be achieved for movements up to 18 cm.

The missing part of the station is going to be completed in the early 2015, after the final technological choice of the photosensor will be made.

REFERENCES

[1] ADAM J. *et al.*, *Phys. Rev. Lett.*, **110** (2013) 201801.
[2] BERTL W. *et al.*, *Eur. Phys. J. C*, **47** (2006) 337.
[3] MARCIANO WILLIAM J. *et al.*, *Ann. Rev. Nucl. Part. Sci.*, **58** (2008) 315.
[4] BARTOSZEK L. *et al.*, *Mu2e Technical Design Report*, http://arxiv.org/abs/1501.05241.
[5] KUTSCHKE ROBERT K., *J. Phys.: Conf. Ser.*, **396** (2012) 022028.
[6] CORDELLI M. *et al.*, *J. Phys.: Conf. Ser.*, **404** (2012) 012027.
[7] THORLABS, http://www.thorlabs.de/thorcat/13000/PDA25K-EC-Manual.pdf.
[8] ALAN SILL for the CDF COLLABORATION, *Nucl. Instrum. Methods A*, **447** (2000) 18.
[9] GECKODRIVE, http://www.geckodrive.com/g203v-rev-7.
[10] MICROCHIP, dsPIC30F0314/4013 data sheet,
     http://www.microchip.com/downloads/en/DeviceDoc/70138G.pdf.
[11] MICROCHIP, Explorer 16 board data sheet,
     http://www.microchip.com/Developmenttools/ProductDetails.aspx?PartNO=DM240001.